

# Multichannel Piezo-Ultrasound Implant with Hybrid Waterborne Acoustic Metastructure for Selective Wireless Energy Transfer at Megahertz Frequencies

Laiming Jiang,\* Gengxi Lu, Yang Yang, Yang Xu, Fangjie Qi, Jiapu Li, Benpeng Zhu,\* and Yong Chen\*

Ultrasound energy transfer (UET) is developed and integrated into various bioelectronics with diagnostic, therapeutic, and monitoring capabilities. However, existing UET platforms generally enable one function at a time due to the single ultrasound channel architecture, limiting the full potential of bioelectronics that requires multicontrol modes. Here, a multichannel piezo-ultrasound implant (MC-PUI) is presented that integrates a hybrid waterborne acoustic metastructure (HWAM), multiple piezo-harvesters, and a miniaturized circuit with electronic components for selective wireless control via ultrasound frequency switching. The HWAM that utilizes both a 3D-printed air-diffraction matrix and a half-lambda Fabry–Perot resonator is optimized to provide the advantage of ultrasound selectivity at megahertz frequencies. Complying with U.S. Food and Drug Administration regulations, frequency-controlled multifunctional operations, such as wireless charging ( $\approx 11.08 \mu\text{W}$ ) at 3.3 MHz and high-sensitivity wireless switch/control (threshold  $\approx 0.55 \text{ MPa}$ ) of micro-light-emitting diode/motor at 1 MHz, are demonstrated *ex vivo* using porcine tissue and *in vivo* in a rat. The developed MC-PUI enhances UET versatility and opens up a new pathway for wireless implant design.

## 1. Introduction

Advancements in biomedical electronic devices (BEDs), such as cardiac pace-makers,<sup>[1]</sup> cardioverter defibrillators,<sup>[2]</sup> neurostimulators,<sup>[3]</sup> and visual prosthesis,<sup>[4]</sup> have promoted enormous benefits for health and quality of life. However, the development of long-lasting uninterrupted power sources remains a massive challenge for realizing the next generation of personalized BEDs that are multifunctional, long-lived, and highly untethered. Although recent advances in wireless technologies have attempted to alleviate the limitations relating to the tethered approach and expand their functionality,<sup>[3,5–7]</sup> current technologies primarily rely on battery-powered or battery-free approaches. The former approach provides a stable stand-alone power solution but requires periodic battery replacement to ensure sustainable operation, resulting in nonnegligible risks and burdens.<sup>[8]</sup> The

latter strategy is mainly executed by electromagnetic waves and self-powered technologies. Most wireless implantable systems use electromagnetic waves for power transmission and communication, but they raise safety concerns and couple inefficiently at the centimeter level deep in the tissue.<sup>[9]</sup> Self-powered technologies, such as triboelectric nanogenerators,<sup>[10]</sup> piezoelectric nanogenerators,<sup>[11]</sup> biofuel cells,<sup>[12]</sup> and thermal energy harvesters,<sup>[13]</sup> convert energy from the human body into electricity to provide a sustainable power source. Nevertheless, these systems generally suffer from limitations associated with the specific implant locations and uncertain output power, thus restricting their full potential.


As a promising energy transfer strategy, ultrasound energy transfer (UET) that utilizes propagating ultrasound (US) waves to transfer energy has been developed and integrated into various bioelectronic systems with wireless functions.<sup>[6,7,9,14,15]</sup> US has long been used as a safe and noninvasive tool to diagnose, sense, and monitor diverse diseases and physical conditions.<sup>[16,17]</sup> Compared with harvesting energy from the human body, portable external US sources can offer tunable, programmable, and long-term sustainable energy transfer *in vivo*, independently of environment location or transparency.<sup>[6]</sup>

L. Jiang, Y. Xu, F. Qi, Y. Chen  
Epstein Department of Industrial and Systems Engineering  
Viterbi School of Engineering  
University of Southern California  
Los Angeles, CA 90089, USA  
E-mail: laiming\_jiang@foxmail.com; yongchen@usc.edu

G. Lu  
Alfred E. Mann Institute for Biomedical Engineering  
University of Southern California  
Los Angeles, CA 90089, USA

Y. Yang  
Department of Mechanical Engineering  
San Diego State University  
San Diego, CA 92182, USA

J. Li, B. Zhu  
School of Optical and Electronic Information  
Wuhan National Laboratory for Optoelectronics  
Huazhong University of Science and Technology  
Wuhan 430074, China  
E-mail: benpengzhu@hust.edu.cn

 The ORCID identification number(s) for the author(s) of this article can be found under <https://doi.org/10.1002/adma.202104251>.

DOI: 10.1002/adma.202104251

Piezoelectric and triboelectric US energy harvesters (UEHs) for implants have been demonstrated.<sup>[6,7,14,18]</sup> However, most of these UEHs used a single US channel, which greatly limited system versatility. For example, to meet the extensive requirements for the next generation of personalized BEDs, future systems will require more functions, powerful wireless communication, and multicontrol capabilities, which might be addressed in a frequency-selectable multichannel UET strategy. Recently, several advances have attempted to mimic the basilar membrane of human cochlea used for multiresonant piezoelectric acoustic sensors.<sup>[19–21]</sup> However, their designs are mainly applied for air medium transmission and audible audio range ( $f < 20$  kHz), well below the usual range ( $f \sim 1$ – $18$  MHz) of medical US for procedural guidance.<sup>[22]</sup> Implantable multichannel UET systems that combine wireless charging and wireless control capabilities have not been demonstrated at megahertz (MHz) frequencies. To achieve these desirable capabilities, well-designed device structures, new frequency control methods, and circuit layouts for tuning the driving frequencies are needed for transferring the US power effectively and exclusively to multiple harvesters.

Acoustic metamaterials, arising from artificial materials or structures, show a remarkable ability to manipulate acoustic waves for specific purposes.<sup>[23]</sup> They have extended the wave manipulation functionalities beyond those found in nature, including high-efficient sound reflection,<sup>[24]</sup> nondiffraction beams,<sup>[25]</sup> asymmetric transmissions,<sup>[26]</sup> subwavelength imaging and focusing beyond the diffraction limit,<sup>[27]</sup> acoustic cloakings,<sup>[28]</sup> and acoustic diodes.<sup>[29]</sup> The ability to tailor wave phase and/or amplitude also leads to acoustic holograms.<sup>[30]</sup> Although acoustic metamaterials have rapidly grown for almost 20 years, the practical applications of acoustic metamaterials are still an overarching challenge, especially in the area of medical US including therapeutics, imaging, and monitoring.<sup>[31]</sup> On the one hand, the subwavelength structure challenges the fabrication of acoustic metamaterials in the MHz-level US with wavelengths in micrometer (e.g., 3 MHz US in water has 500  $\mu$ m wavelength). On the other hand, diverse acoustic metamaterials have an important assumption of the rigid boundary between metamaterials structures and the background medium. This assumption can be easily realized in airborne acoustic metamaterials but becomes inaccurate in water/tissue because water/tissue has a lower contrast in acoustic impedance compared with most solid materials.

To overcome these challenges, we propose a multichannel piezo-ultrasound implant (MC-PUI) with a hybrid waterborne acoustic metastructure (HWAM) that utilizes both an air-diffraction matrix (ADM) and a half-lambda Fabry–Perot resonator (FPR) to select the transmittable US waves. Consequently, multicontrol capabilities at MHz frequencies can be realized. Mask-image-projection-based stereolithography (MIP-SL), a 3D printing technology, was used to assist in processing the HWAM as the core artificial frequency selector. The newly designed MC-PUI integrates multiple piezo-composite harvesters, an artificial frequency selector, and commercialized electronic components into a miniaturized circuit, which can be wirelessly powered by a rechargeable system at 3.3 MHz and wirelessly controlled at 1 MHz. This integration not only allows minimalistic device design without requiring bulky architec-

ture for reliable frequency operation, but also enables highly versatile wireless control such as in future cardiovascular and neuroengineering devices. Systematic studies, including principle exploration, structural optimization, ex vivo and in vivo demonstrations of wireless charging and switch/control, and safety discussion, were performed to evaluate its potential applications. The developed MC-PUI significantly promotes the frequency-tunable multioperations of UET and opens up a previously unexplored pathway for wireless implantable device design.

## 2. Results and Discussion

### 2.1. Design, Layout, and Working Principle of the MC-PUI

**Figure 1a** shows a conceptual illustration of the MC-PUI for selective wireless power transfer and control in biomedical implants. The implanted MC-PUI can be selectively activated through ultrasonic excitation at different frequencies to achieve these specific functions. **Figure 1b** shows a schematic diagram of the wirelessly rechargeable and frequency-controlled MC-PUI. The miniaturized device incorporates four main functional parts via ingenious circuit design to provide exceptional capabilities (**Figure 1b** and **Figure S1**, Supporting Information): i) a multichannel piezo-harvester with HWAM for selective energy harvesting, ii) an energy storage circuit with a full-wave rectifier and a rechargeable capacitor for wireless charging, iii) a switch/control circuit with two transistors for US wireless control, and iv) microelectronic devices (micro-light-emitting-diode ( $\mu$ -LED, red) and micro-motor ( $\mu$ -motor)) for the demonstration of the frequency-controlled switch. The usual range of medical US for procedural guidance is 1–18 MHz.<sup>[22]</sup> The selection of operating frequencies (3.3 and 1 MHz) in our work is therefore based on the considerations of safety and transmission efficiency (for the detailed discussion, see Note S1, Supporting Information). A confocal dual-frequency US transmitter was designed and fabricated as the external acoustic source. The multichannel piezo-harvester with a concentric circular structure (circular UEH 1: diameter  $\approx 2.7$  mm; ring UEH 2: inner diameter  $\approx 3$  mm, outer diameter  $\approx 6.2$  mm) as the core component helps harvest wireless US energy to form electricity. In particular, a structurally optimized HWAM composed of both a 3D-printed ADM and a half-lambda FPR was conformally designed on the UEH 2, thus enabling selective US harvesting (**Figure 1c** and **Figure S2**, Supporting Information).

The circuit diagram of the overall MC-PUI is illustrated in **Figure 1d**. Both an ultrasonic wireless charging system (**Figure 1d**, right) and a frequency-dependent switch/control system (**Figure 1d**, left) are designed to match the demand for multicontrol. In the charging system part, the output produced by UEH 1 is rectified by a full-wave rectifier and then stored in a capacitor. This process is driven by 3.3 MHz US. In the frequency-dependent switch/control system part, an amplifier circuit composed of UEH 2 and two transistors is used to connect the energy storage system and the microelectronic devices that need to be powered, realizing highly selective control of power through US frequency switching. UEH 2 only responds favorably to 1 MHz US due to the configuration of HWAM.

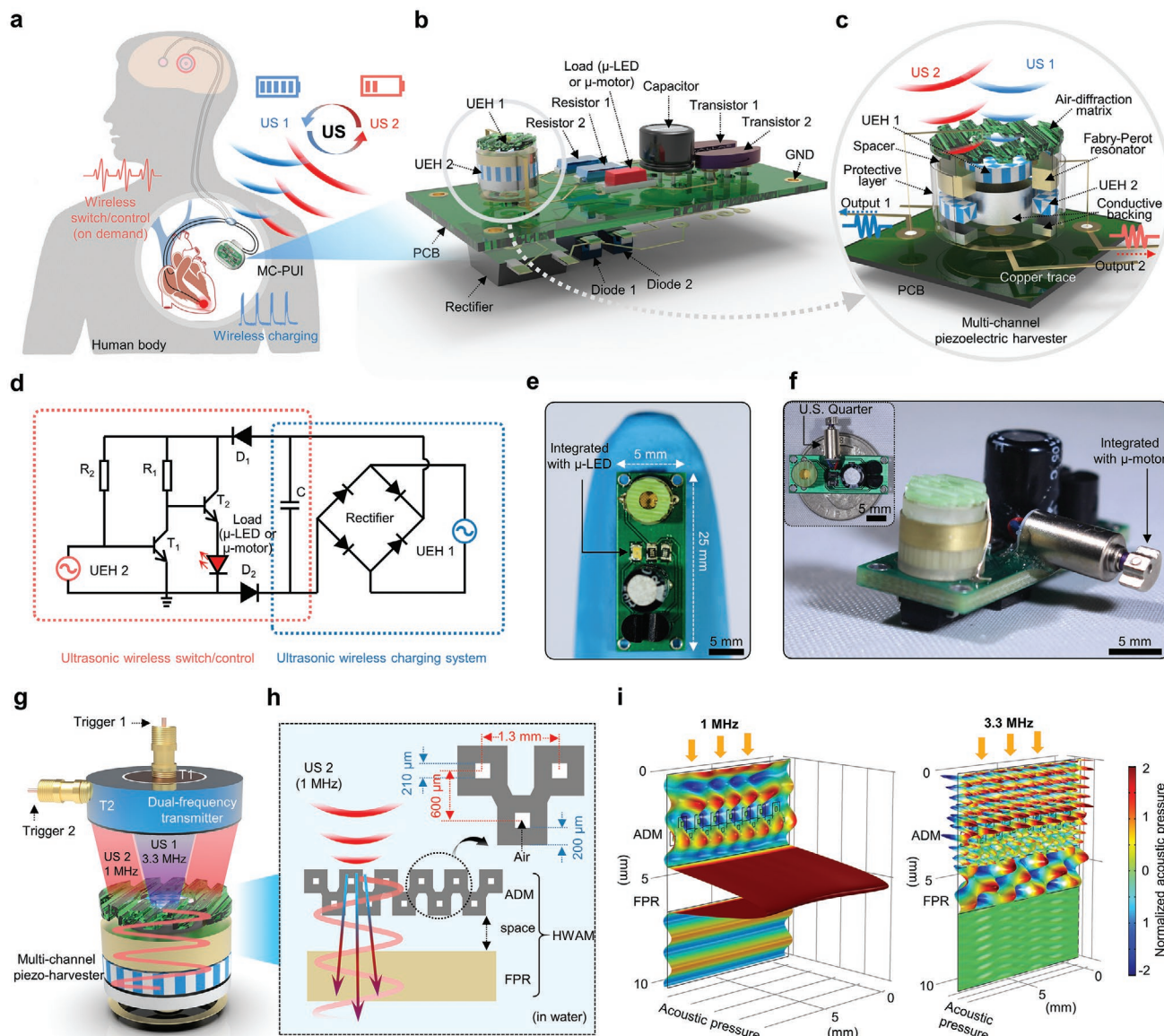


**Figure 1.** Schematics and principle of the MC-PUI for selective wireless energy transfer. a) Schematic showing the MC-PUI for a potential multi-functional implantable device, which possesses integrated functions of wireless charging and wireless switch/control under ultrasonic excitation of different frequencies. b) Schematic of the MC-PUI device integrated on a PCB using a series of electrical and acoustic components, with key components labeled. c) Exploded schematic of the multichannel piezo-harvester with HWAM, a key component of the MC-PUI. d) Circuit diagram of the MC-PUI device, including an ultrasonic wireless charging system and a frequency-dependent wireless switch/control system. e,f) Optical micrographs showing the fabricated MC-PUI devices integrated with a e) micro-light-emitting-diode ( $\mu$ -LED) and f) a micro-motor ( $\mu$ -motor). g) Schematic showing the multi-channel piezo-harvester being excited by US of different frequencies. h) A confocal dual-frequency transducer with center frequencies of 3.3 and 1 MHz was designed and manufactured to be the external ultrasonic transmitter. i) Schematic of the HWAM structure and the corresponding lattice parameters of 3D-printed ADM. j) Acoustic field comparison between the numerical simulations with HWAM at the frequencies of 1 and 3.3 MHz, respectively. 1 MHz US effectively penetrates the HWAM, while the 3.3 MHz US shows low transmission. The acoustic pressure is normalized to the incident value.

Here, the strategy of integrating the rechargeable energy storage system with a wireless frequency-dependent switch/control provides unique capabilities superior to existing battery-powered and self-powered wireless technologies.<sup>[32]</sup> One of the most important attributes of this design is that the wireless recharging function eliminates the requirement for periodical battery replacement. The wireless switch/control allows users to ultrasonically operate implants, thereby providing opportunities

for noninvasive chronic in vivo operation. Moreover, the devices powered by an integrated energy storage system enable stable operation independent of power settings and environment, making their use more versatile. Figure 1e,f shows the resulting devices assembled on a custom printed circuit board (PCB). The device measures 25 mm long  $\times$  10 mm wide  $\times$  12 mm height and has a weight of  $\approx$  3.3 g. The lightweight and compact electronic design facilitates the integration of the MC-PUI inside the body.



The entire surface of the device is uniformly deposited with parylene-C (30  $\mu\text{m}$ ) as encapsulation and biocompatible passivation (for the detailed fabrication process, see the Experimental Section). Some potential scenarios for its use in implantable bioelectronics are schematically illustrated in Figure 1a, such as integration into cardiac pacemakers and neurostimulators.

Although piezoelectric harvesters generally receive the optimal output at the resonant frequency, their relatively broad receiving frequency response limits applications in highly selectable transfer, especially in a narrow frequency band (Figure S3, Supporting Information). Therefore, the HWAM as an artificial frequency selector utilizing both ADM and Fabry–Perot (FP) resonance<sup>[33]</sup> was designed and manufactured to select the transmittable frequency of US waves (Figure 1g,h). A half-lambda FP resonator (FPR) with a high impedance mismatch was first chosen for the artificial frequency selector due to its simple structure and easy fabrication. Under normal incidence, FPR's transmission coefficient ( $T_1$ ) of acoustic intensity can be described as<sup>[33]</sup>

$$T_1 = \frac{4R_1R_3}{(R_1 + R_3)^2 \cos^2(k_2D) + \left(R_2 + \frac{R_1R_3}{R_2}\right)^2 \sin^2 k_2D} \quad (1)$$

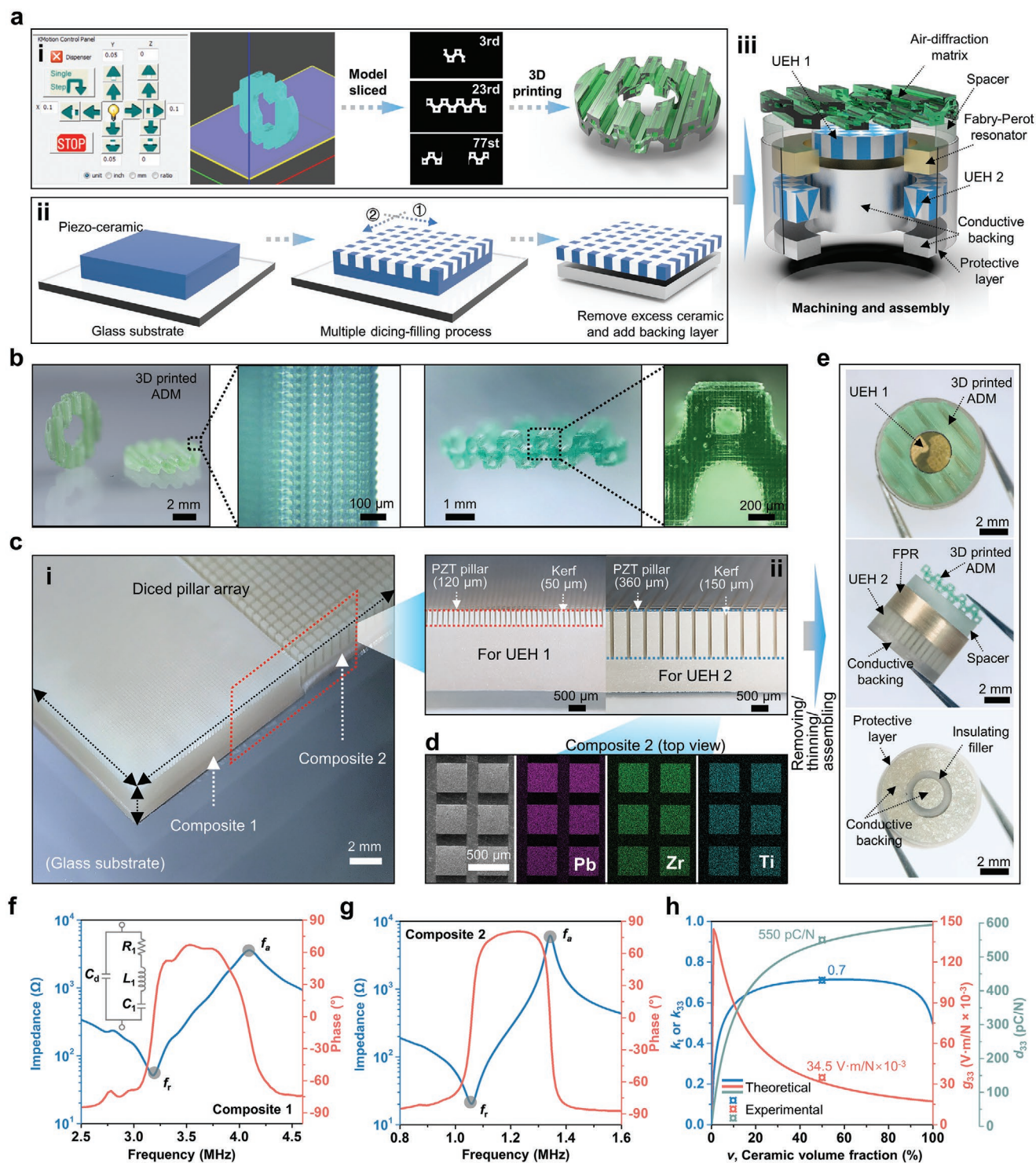
where  $R_n$  is the acoustic impedance of the  $n$ th layer,  $D$  is the thickness of the resonator,  $k_2$  is the wave vector in the FPR (Note S2, Supporting Information). Its frequency dispersion curve is shown in Figure S4 (Supporting Information). The peaks of transmission coefficient are observed at resonant frequencies  $f = m \frac{c}{2D}$  ( $m = 1, 2, 3 \dots$ ). Although the FPR can filter out a large portion of US waves in the frequency domain, it still has two defects that need to be improved. First, the bandwidth of the FP resonator is still relatively large ( $\approx 26.95\%$ ) even if the brass is chosen, which has a large acoustic impedance mismatch among common solid materials (Figure S5, Supporting Information). Second, FPR has multiple resonant frequencies in a tight frequency band, but only one frequency is desired in our application. Thus, the ADM is stacked to the FPR to narrow the bandwidth further and reduce the transmission coefficient in undesired FP resonant frequencies. The design of the ADM is based on Bragg diffraction, which was first proposed by L. Bragg to explain the X-ray diffraction in crystals.<sup>[34]</sup> Different from locally resonant phononic crystals with sub-wavelength structures,<sup>[35]</sup> the lattice constant of periodic structures based on Bragg's diffraction is in the same level of wavelength, which is defined by the Bragg's law  $n\lambda = 2a \sin \theta$ , where  $a$  is the lattice constant and  $\theta$  is the angle of incidence (Figure S6, Supporting Information). The lattice structure of the designed matrix is shown in Figure 1h. The parameters of ADM are deliberately designed to leave the peak of the dispersion curve at 1 MHz (Figure S7, Supporting Information; and the detailed analysis in Note S3, Supporting Information). The air scattering is formed by the 3D-printed microchannels. In Figure 1i, the simulated acoustic fields of HWAM are compared at different frequencies. 1 MHz US effectively penetrates the HWAM, while the 3.3 MHz US shows low transmission. Thus, the HWAM designed by combining hybrid resonance modes exhibits the advantage of frequency high-selectivity at MHz-level.

## 2.2. Structure Optimization using 3D Printing and Dicing-and-Filling Fabrication Strategies

The multichannel piezo-harvester with HWAM is the key component to realize selective energy transfer. First, properties of acoustic metamaterials usually arise from sophisticated structure, with techniques such as the controlled fabrication of small inhomogeneities to enact effective macroscopic behavior.<sup>[23,36]</sup> Additive manufacturing (a.k.a., 3D printing) is a powerful fabrication tool to address this challenge and build an artificial frequency selector made of a periodic arrangement of scatterers.<sup>[37–39]</sup> Here, the MIP-SL-based 3D-printing technology was adopted to build the ADM with periodic microchannel matrix due to its high resolution (Figure 2a -i and Figure S8, Supporting Information) (for the detailed fabrication process see the Experimental Section).<sup>[40,41]</sup> The images in Figure 2b and Figure S9 (Supporting Information) show that the ADM model is successfully built with a ring structure of an inner diameter of 3 mm, an outer diameter of 6.5 mm, and a thickness of 1.22 mm, with periodic microchannels ( $210 \pm 10 \mu\text{m}$ ) stacking within two layers. Second, in a series of common solid materials, brass was selected as the FPR due to its large acoustic impedance, moderate acoustic velocity, and ease of processing (Figure S4 and Table S1, Supporting Information). The final machined ring brass FPR with a thickness of  $\approx 2.2$  mm and the 3D-printed ADM were then assembled into an HWAM that was physically attached to the front of UEH 2 to control and manipulate transmitted US (Figure 2a -iii and Figure S10, Supporting Information).

As the core component of acoustic-electric conversion, lead zirconate titanate (PZT) ceramic was chosen for its high electromechanical coupling coefficient and relatively low loss tangent, enabling high power harvesting efficiency. Then, the bulk ceramic was further processed into 1–3 composite via the dicing-and-filling method (Figure 2a -ii). Compared to the isotropic bulk PZT, the epoxy in the anisotropic 1–3 composite confines the transverse vibration of the PZT pillars and concentrates the energy on the longitudinal vibration. That is, the PZT pillars in the 1–3 composite vibrate in the fundamental length longitudinal 33-mode with higher coupling coefficient  $k_{33}$  (Figure S11, Supporting Information),<sup>[42,43]</sup> providing more efficient voltage and power harvesting. A thickness-to-width aspect ratio of the piezo-pillar higher than 2 is required to ensure the vibration of each piezo-pillar is dominant in the longitudinal 3–3 direction. Therefore, one ceramic/epoxy 1–3 piezo-composite with a pillar width of 120  $\mu\text{m}$ , a kerf of 50  $\mu\text{m}$ , and a thickness of 450  $\mu\text{m}$  was designed and further manufactured into the circular UEH 1 with a diameter of 2.7 mm. Another composite with a pillar width of 360  $\mu\text{m}$ , a kerf of 150  $\mu\text{m}$ , and the thickness of 1.5 mm was also fabricated for the ring UEH 2 with an inner diameter of 3 mm and an outer diameter of 6.2 mm (Figure 2c,d and Figure S12, Supporting Information). The 1–3 composites satisfy a thickness-to-width aspect ratio of  $\approx 4$  and a ceramic volume fraction of  $\approx 50\%$ , ensuring their efficiency as the acoustic-electric conversion elements. Finally, the machined harvesters and the processed HWAM were assembled together to construct into the multichannel piezo-harvester (Figure 2e). Polarization–electric field ( $P$ – $E$ ) hysteresis loops of PZT bulk and 1–3 composite samples were measured, as shown





in Figure S13 (Supporting Information). The epoxy polymer is without ferroelectric polarization, so the role of epoxy decreases the total  $P$ - $E$  effect of the 1-3 composites; therefore, the average value of remnant polarization  $P_r$  is smaller than the bulk PZT ceramic. The electrical equivalent capacitance, inductance, and resistance describe the electrical effects of the mechanical motion of the piezoelectric elements (Figure 2f, left inset and Note S4, Supporting Information).<sup>[44]</sup> The resonance frequency  $f_r$  of the harvester is defined by the following formula

$$f_r = \frac{N_t}{t} = \frac{1}{2t} \sqrt{\frac{(1-\sigma)}{\rho S_{11}^E (1+\sigma)(1-2\sigma)}} \quad (2)$$

where  $N_t$  is the thickness mode frequency constant,  $t$  is the thickness of the piezoelectric layer,  $\rho$  is the density,  $\sigma$  is the Poisson's ratio, and  $S_{11}^E$  is the elastic compliance of the piezoelectric material. The resonance frequencies of the as-manufactured 1-3 composites are 3.19 MHz (for composite 1) (Figure 2f) and 1.06 MHz (for composite 2) (Figure 2g), respectively, corresponding to the designed ultrasonic operating frequencies (3.3 and 1 MHz) for selective control of the MC-PUI. Both the electromechanical coupling coefficient ( $k_{33} \sim 0.7$ ) and piezoelectric voltage coefficient ( $g_{33} \sim 34.5 \times 10^{-3} \text{ V m N}^{-1}$ ) were significantly augmented in the fabricated 1-3 composites through the suppression of the shear vibrating modes (Figure 2h),<sup>[45]</sup> thus ensuring their enhanced output efficiency (Figure S14, Supporting Information). The theoretical prediction of the values was performed based on the parallel and series model proposed by Unsworth and Chan (Note S5 and Figure S15, Supporting Information).<sup>[46]</sup> Some key electrical and acoustic parameters of the bulk PZT ceramic and as-manufactured 1-3 composites are summarized in Table S2 (Supporting Information).

### 2.3. Simulation and Characterization of the HWAM for Selective Wireless Energy Transfer

1-3 piezo-composites are superior candidates for US-induced energy harvesting. The output voltage  $V$  can be derived as the following formula<sup>[47]</sup>

$$V = -\frac{Pk_{33}^2}{e_{33}(1+k_{33}^2)} \frac{Z_L}{\xi \cot(\xi h)(Z_0 + Z_L)} \quad (3)$$

where  $\xi$ ,  $Z_L$ ,  $Z_0$ , and  $h$  are the wavenumber, load resistor, electric impedance, and thickness of the piezo-harvester, respectively.  $k_{33}$  is the electromechanical coupling coefficient of the piezoelectric material and can be expressed as  $k_{33}^2 = \frac{e_{33}^2}{\epsilon_{33}C_{33}}$ , in which  $C_{33}$ ,  $\epsilon_{33}$ , and  $e_{33}$  are the effective elastic, dielectric, and piezoelectric constants, respectively. 1-3 composite structures were thus designed and manufactured to enhance the output voltage.  $P$  is the ultrasonic pressure applied to the piezo-harvester and directly induces the electrical output. Theoretically, the output voltage can be regulated by controlling and manipulating the ultrasonic transmittance, which is highly dependent on the designed acoustic structure and ultrasonic frequency. First, we demonstrated numerically how the HWAM real-

ized the frequency-dependent regulation of output voltage. In Figure 3a,b, the simulated acoustic fields through the HWAM and the corresponding induced piezoelectric output are compared. When  $f = 1$  MHz, ultrasonic waves effectively pass through the HWAM and correspondingly induce a high piezoelectric potential. However, when  $f = 3.3$  MHz, HWAM effectively blocks the transmission of ultrasonic waves, and a weak piezoelectric potential is induced. We further analyzed the bandwidth that is defined as the normalized transmission coefficient of acoustic pressure larger than  $-3$  dB. For the FPR alone, it is demonstrated that the bandwidth becomes narrower as the acoustic impedance mismatch becomes more significant. For example, tungsten, which has the largest acoustic impedance among common natural materials, can provide a bandwidth of 9.35% (Figure S5, Supporting Information). As a comparison, the HWAM design theoretically provides a narrower bandwidth of  $\approx 4\%$  near 1 MHz, differing from a single FPR or ADM structure (Figure 3c and Figure S7, Supporting Information). Transmission efficiencies of 87% and 5% were calculated at 1 and 3.3 MHz, respectively (Figure 3c). We then experimentally measured the transmission efficiency of HWAM to US within the frequency range from 0.3 to 4 MHz, where the transmission efficiencies were  $\approx 83\%$  and  $\approx 8\%$  at 1 and 3.3 MHz, respectively (Figure 3d). HWAM has a strong frequency selectivity of US. The fluctuation of the experimental values may be associated with acoustic dissipation and the processing deviation of the microstructures.

To further verify the selective ultrasonic energy transfer of HWAM, we experimentally manufactured two piezo-harvesters (resonant frequency  $\approx 1$  MHz) with and without HWAM. We then measured their output voltages, as shown in Figure 3e. An apparent attenuation ( $\approx -28$  dB) in voltage amplitude was detected for the harvester configured with HWAM as the US frequency was switched from 1 to 3.3 MHz. This frequency-dependent voltage attenuation is mainly attributed to two aspects, one is the frequency response of the piezoelectric layer itself, and the other is the narrowed bandwidth effect of HWAM. The piezoelectric potential was first generated between the upper and lower surfaces when the piezoelectric layer is ultrasonically deformed. Induced charges then flowed through the external circuit to screen the piezoelectric potential, thereby resulting in alternating signals of current and voltage under a dynamic ultrasonic field. As analyzed above, HWAM effectively blocked the ultrasonic transmission into the piezoelectric layer at 3.3 MHz. Thus an attenuated output was detected. Figure 3f-h shows the waveform comparison between the trigger signal to the external transmitter and the output signals from the piezo-harvesters driven by the corresponding transmitted US at 1 MHz. All the sine wave periodicities ( $\approx 1 \mu\text{s}$ ) of the output signals and the trigger signal are temporally identical. That is, frequency is consistent (Figure 3g). However, compared with the trigger signal, the output signals possess a wider waveform with a time delay and a typical ring-down phase (Figure 3g,h), which is a result of the US traveling and interface reflection. In addition, a shorter time delay was observed in the output signal generated by the harvester configured with HWAM due to much larger acoustic velocity in brass ( $\approx 4400 \text{ m s}^{-1}$ ) and polymer resin ( $\approx 2500 \text{ m s}^{-1}$ ) than in water ( $\approx 1540 \text{ m s}^{-1}$ ) (Figure 3g). Considering that the ultrasonic



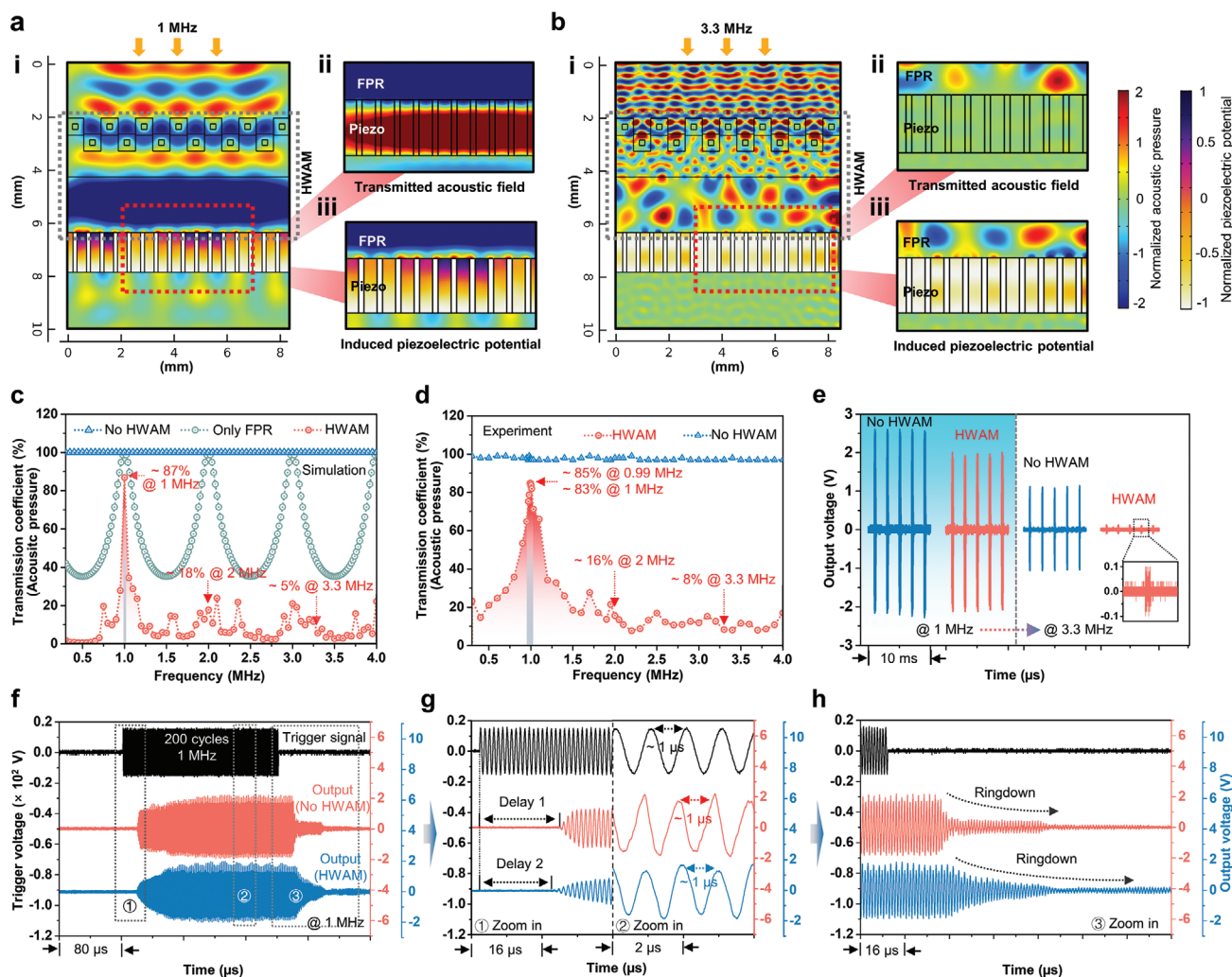


**Figure 3.** Simulation and characterizations of the MC-PUI with HWAM. a,b) Comparisons of acoustic field and corresponding induced piezoelectric potential between the numerical simulations with HWAM at the frequencies of 1 and 3.3 MHz, respectively. The acoustic pressure is normalized to the incident value. c) Frequency response comparison between the numerical simulations with and without FPR and HWAM. d) Frequency response comparison between the experimental measurements with and without HWAM. e) Output voltage comparison between the experimental measurements with and without HWAM under US frequencies at 1 and 3.3 MHz. f–h) Trigger signals to the US transmitter and the output signal from the piezo-harvesters with and without HWAM, driven by 1 MHz sine waves. The output signals exhibit a g, left) time delay, g, right) frequency consistency, and h) ringdown phase.

transmission process may produce a friction effect on the device, other two harvesters were further prepared, one of which contained an unpoled piezoelectric element and the other without piezoelectric material. No reliable signals were observed from these two harvesters under ultrasound excitation (Figure S16, Supporting Information). The results further verify that the US-induced output signals are from charges generated by the piezoelectric effect.

#### 2.4. Ex Vivo Demonstration of the MC-PUI for Wireless Charging at 3.3 MHz

This work aims to develop a frequency-controlled wireless multifunctional system for bioelectronic implants. We evaluated the MC-PUI ex vivo under porcine tissue (Figure 4a–c), which

is compositionally and anatomically similar to human tissue. Figure 4c and Figure S17 (Supporting Information) show the ex vivo experimental setup, in which the customized dual-frequency transmitter as the wireless US source was mounted to a movable holder and the MC-PUI device as US scavenger was placed under the porcine tissue. The dual-frequency transmitter with 3.3 and 1 MHz operation frequencies was designed to integrate two confocal piezo-transducers through Krimholtz, Leedom, and Mattaei (KLM) simulation and a simple assembly process (see the Experimental Section and Figures S18–S20, Supporting Information) to allow a facile and rapid frequency switch with a portable dimension. First, the MC-PUI implant can be recharged wirelessly via UEH 1 that is excited by the transmitted US at 3.3 MHz (Figure 4d), while UEH 2 as a switch remains off. Figure 4e,f shows the trigger signal to transmitter 1 and the output signal from UEH 1 driven by the



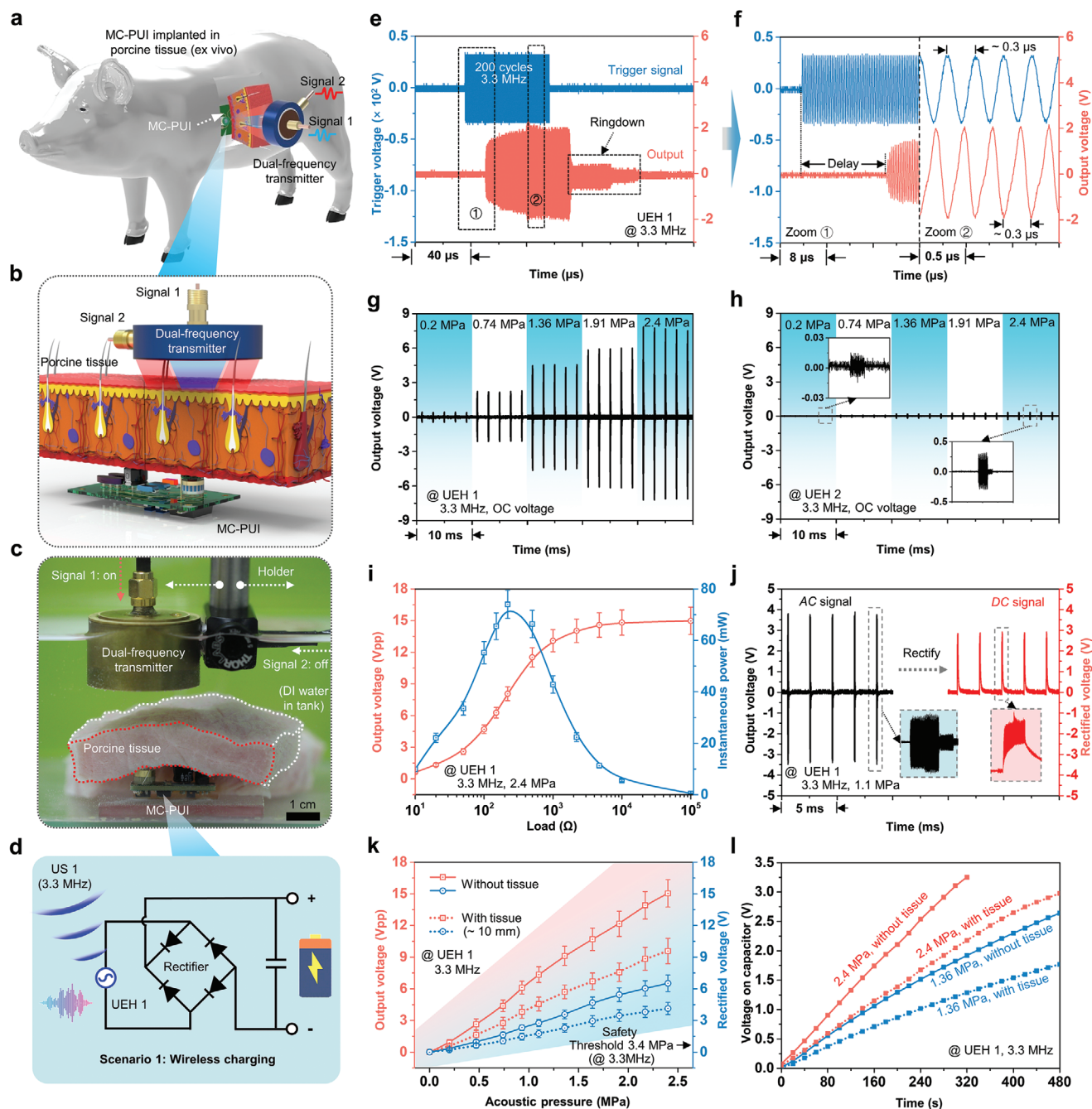


**Figure 4.** Ex vivo characterizations of the charging performance of MC-PUI at 3.3 MHz. a,b) Schematic diagram of the ex vivo model showing the implanted MC-PUI device. c) Optical image showing the testing setup with the MC-PUI device implanted under porcine tissue. d) Circuit model showing the scenario of MC-PUI for wireless charging. e,f) Trigger signal to US transmitter 1 and the output signal from the UEH 1 driven by the corresponding transmitted 3.3 MHz US. The output signal exhibits a e) ringdown phase, f, left) a time delay, and f, right) frequency consistency. g,h) Output voltage amplitudes of g) UEH 1 and h) UEH 2 of the MC-PUI, induced by 3.3 MHz US at different input acoustic pressures. UEH 1 exhibits obvious superiority in voltage output. i) Instantaneous power of UEH 1 in response to diverse loads, showing optimal power near 200  $\Omega$ . j) Output voltage amplitudes before (left) and after (right) rectification of UEH 1 driven by 3.3 MHz US. k) Output voltage variation of UEH 1 with input acoustic pressures, showing a linear relationship. l) The charging time dependence of voltage on a 220  $\mu$ F capacitor under different acoustic pressures, showing a faster-charging capacity obtained under higher acoustic pressure. The repeat cycle number of the 3.3 MHz US is 200.

corresponding transmitted 3.3 MHz US. The periodicity ( $\approx 0.3 \mu$ s) of the output signal and the trigger signal is temporally identical, i.e., frequency is consistent. As mentioned above, compared with the trigger signal, the output signal possesses a

longer pulse length with a time delay and a typical ringdown phase (Figure 4e), which is a result of the US traveling and interface reflection and further demonstrates the fact that the output voltage is induced by the propagating US.

Figure 4g shows open-circuit (OC) voltage amplitudes of UEH 1 induced by 3.3 MHz US at different incident acoustic pressures. With increasing acoustic pressure, the OC voltage amplitude of UEH 1 increases linearly with a piezoelectric sensitivity of  $\approx 6.3 \mu\text{Vpp Pa}^{-1}$ , reaching  $\approx 15.05 \text{ Vpp}$  as the incident acoustic pressure is 2.4 MPa; meanwhile, the amplitude of UEH 2 does not exceed 0.6 Vpp (Figure 4h), showing good shielding of 3.3 MHz US. The instantaneous power of UEH 1 delivered to the load was then evaluated by measuring the voltage amplitudes under various external loads ranging from 10  $\Omega$  to 100 k $\Omega$ . The peak of the delivered power ( $\approx 74 \text{ mW}$ ) was obtained at the incident acoustic pressure of 2.4 MPa and a load of  $\approx 200 \Omega$ , close to its internal electrical impedance, as shown in Figure 4i. In this work, the US transmitter was designed to be a focused architecture. Compared with a planar transmitter, the energy generated from the focused piezo-architecture is focused into a narrow area through the constricted acoustic beam (Figure S21, Supporting Information), which not only enhances the magnitude but also reduces energy dissipation caused by the divergence of the acoustic beam. Therefore, the optimal output is obtained near the focal point (Figure S22, Supporting Information). Additionally, the standing wave effect also affects the device output. The fluctuation of the output voltage along the axial direction was observed (Figure S23, Supporting Information).

Output AC signals of UEH 1 were rectified into general DC signals through a full-wave bridge rectifier circuit so that they can be stored in a capacitor and compatible with general electronics (Figure 4d,j and Figure S24, Supporting Information). Under different test conditions, the linear relationships between the peak voltage and the incident acoustic pressure were plotted in Figure 4k. At 10 mm thickness ex vivo evaluation, UEH 1 produced output voltage amplitudes of  $\approx 63\%$  of the values without tissue. The corresponding rectified voltage is about 4.5 V as the incident acoustic pressure is 2.4 MPa. The decreases in output voltage are primarily due to the acoustic energy dissipation caused by the reflection, absorption, and divergence of the ultrasonic waves in the porcine tissue.<sup>[14]</sup> The rectified DC outputs were then directly stored in a capacitor. The charging rate can be regulated by adjusting the incident acoustic pressure. For example, the voltage of the 220  $\mu\text{F}$  capacitor increased to 3 V in 480 s at 10 mm ex vivo evaluation as the pressure is 2.4 MPa, but only 1.77 V at 1.36 MPa (Figure 4l). Also, the duty cycle of US can also be flexibly adjusted to meet varied charging requirements (Figure S25, Supporting Information). For example, the voltage of the capacitor increased to 3.48 V in 120 s at 2.4 MPa as the repeat cycle number is 2000 (duty cycle  $\approx 30\%$ ) (Figure S26 and Video S1, Supporting Information). The average charging power  $P_{\text{ave}}$  can be calculated by the formula  $P_{\text{ave}} = \frac{CV^2}{2t}$ , where  $C$  is the capacitance,  $V$  is the increased voltage, and  $t$  is the charging time. Consequently, the energy stored in the capacitor increased by 1.33 mJ in 120 s, and the average charging power is  $\approx 11.08 \mu\text{W}$ . The corresponding power level generated could be further improved upon increasing the duty cycle and currently sufficient to charge the batteries of some miniaturized bioelectronics (e.g., pacemakers, required endocardial pacing threshold energy  $\approx 0.377 \mu\text{J}$ ) and to directly power microscopic robots (consuming

$\approx 10 \text{ nW}$ ) and electrical neurostimulators (consuming  $\approx 1 \mu\text{W}$  to 25 mW).<sup>[1,6,48,49]</sup> No apparent attenuation of the output voltage amplitude was observed after ultrasonic excitation for more than 10 min (Figure S25, Supporting Information), indicating the stability of ultrasonic energy transmission.

## 2.5. Ex Vivo Demonstration of the MC-PUI for Wireless Switch/Control at 1 MHz

Ex vivo experiments verified the capability of MC-PUI for wireless charging at 3.3 MHz. We then evaluated the MC-PUI devices in wireless switch/control scenarios, where the ultrasonic frequency was switched from 3.3 to 1 MHz to induce UEH 2 that controls the frequency-dependent switch circuit. To study this scenario, the capacitor has been sufficiently charged to obtain a voltage greater than 3.5 V. As shown in Figure 5a, the switch/control circuit mainly includes UEH 2 and two transistors. The generated electrical output of UEH 2 will turn on transistor 1 ( $T_1$ ) and the related circuit, thereby releasing the energy stored in the capacitor to drive the micro-electronics ( $\mu\text{-LED}$  or  $\mu\text{-motor}$ ). As expected, UEH 2 only responds highly to 1 MHz US due to the configuration of the HWAM. Figure 5b shows output voltage amplitudes of UEH 2 induced by 1 MHz US at different incident acoustic pressures. Like UEH 1, a linear relationship between the peak voltage and the incident acoustic pressure for UEH 2 is established. An output voltage of  $\approx 8.48 \text{ Vpp}$  is obtained as the incident acoustic pressure is 1.39 MPa.

In this wireless switch/control circuit, the sensitivity of ultrasonic control, namely, the base voltage of  $T_1$ , can be regulated by changing the resistance of resistor 2 ( $R_2$ ). The greater the resistance value, the greater the required turn-on voltage. To weaken the influence of 3.3 MHz US on the switch/control, 1 M $\Omega$  resistance was selected for  $R_2$ . Figure 5c,d shows the relationship among the US frequency, incident acoustic pressure, output voltage, and MC-PUI operating status. With increasing the incident acoustic pressure of 1 MHz US, a turn-on voltage of  $\approx 2.5 \text{ Vpp}$  at 0.55 MPa was measured at 10 mm ex vivo evaluation when the  $\mu\text{-LED}$  in the circuit started to be lit up (Video S2, Supporting Information). Higher brightness was observed as the incident acoustic pressure increased (Figure 5e,f), indicating a greater output generated by UEH-2 with a larger current through  $T_2$ . In addition, the 1 MHz-based ultrasonic control also turned on a  $\mu\text{-motor}$  integrated into the MC-PUI. Several turns of rotation of the  $\mu\text{-motor}$  were observed once the incident sound pressure was higher than the threshold (Figure 5g and Video S3, Supporting Information). Meanwhile, the switch/control circuit did not respond to 3.3 MHz US due to the shielding effect of the HWAM structure. Repeated experiments of wireless charging and switch/control show that our MC-PUI functions as designed, thus confirming the potential of MC-PUI for selective and exclusive energy transfer for multifunctional operations. Device design can be further tailored and improved. For example, a series of bioelectronics, including pacemakers, tissue-or neurostimulators, and optogenetic devices, could be integrated into MC-PUI to replace  $\mu\text{-LED}$ /motor for specialized needs. Therefore, the presented technology will help realize the full potential of the near future biomedical systems that require multicontrol capabilities, such

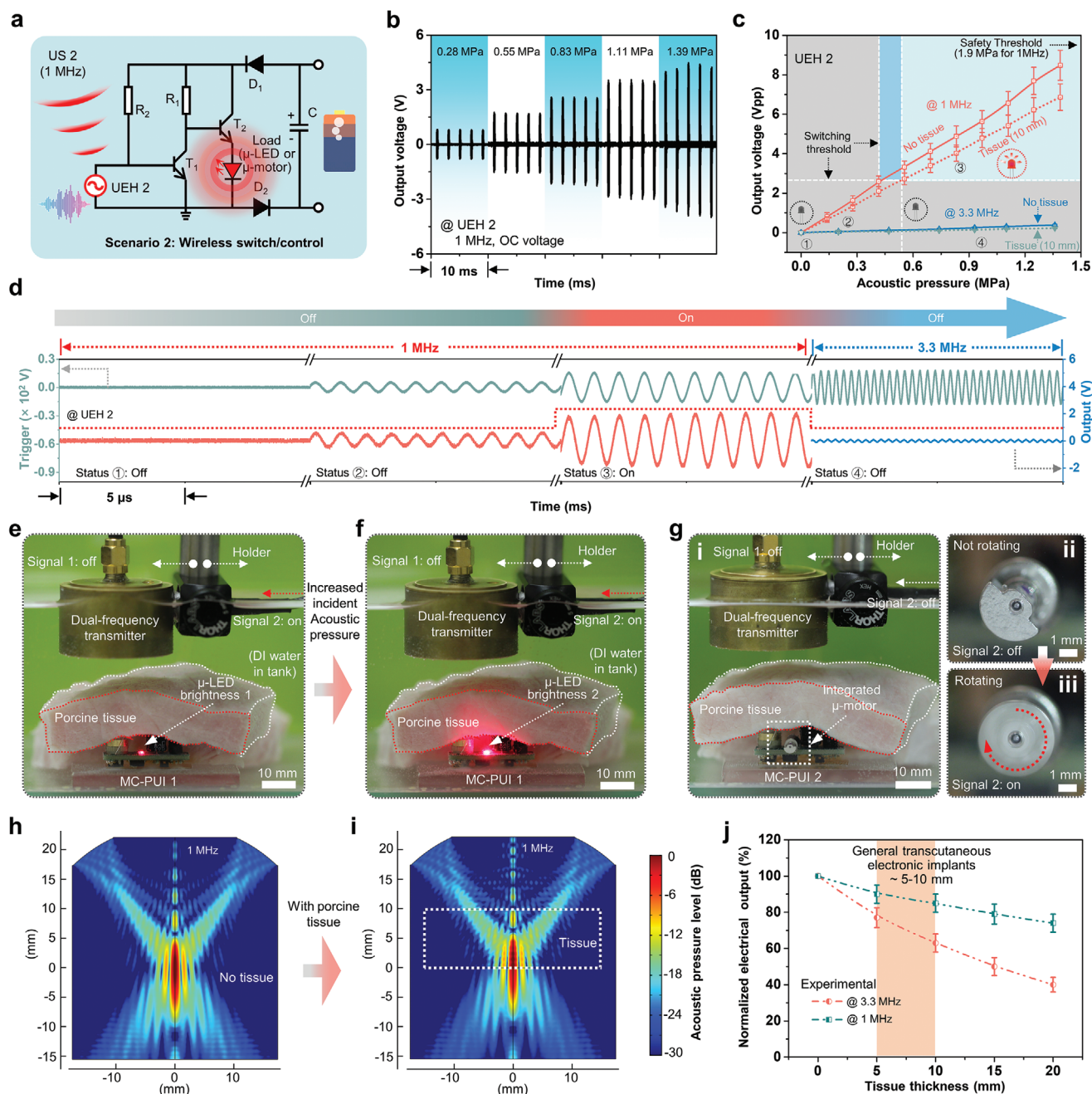


**Figure 5.** Ex vivo evaluation of the wireless switch/control of MC-PUI at 1 MHz. a) Schematic of the MS-PUS as an implantable device for the US-induced wireless switch/control. b) Output voltage amplitudes of UEH 2 as a wireless switch/control in the MC-PUI, induced by 1 MHz US with different input acoustic pressures. c) When the device is in implantation and nonimplantation, the output voltage variation of the switch/control system under different ultrasonic frequencies and input acoustic pressures. The device can be flexibly turned on under 1 MHz excitation, and key parameters are marked to indicate the operational status of the device under different input conditions. d) Output signal waveforms of the switch/control system under increased trigger voltages and different frequencies of 1 and 3.3 MHz. e, f) Optical images of the MC-PUI device in the switch-on status, showing that the μ-LED is activated wirelessly under 1 MHz excitation. g) Optical images showing the μ-motor was activated wirelessly under 1 MHz excitation. h, i) Acoustic field comparison between the numerical simulations h) without and i) with 10 mm porcine tissue at 1 MHz. j) Output voltage comparison of the MC-PUI measured under tissues of different thicknesses.

as in vivo diagnosis and treatment, real-time monitoring, and chronic disease monitoring and feedback (Figure 1a).

To use the MC-PUI as an implantable device, it is necessary to evaluate the efficiency of US transmission through biological

tissue. We further investigated its ex vivo efficiency by measuring the output voltage under various thicknesses of porcine tissues ranging from 0 to 20 mm. The decreases in US energy are primarily due to the acoustic energy dissipation caused



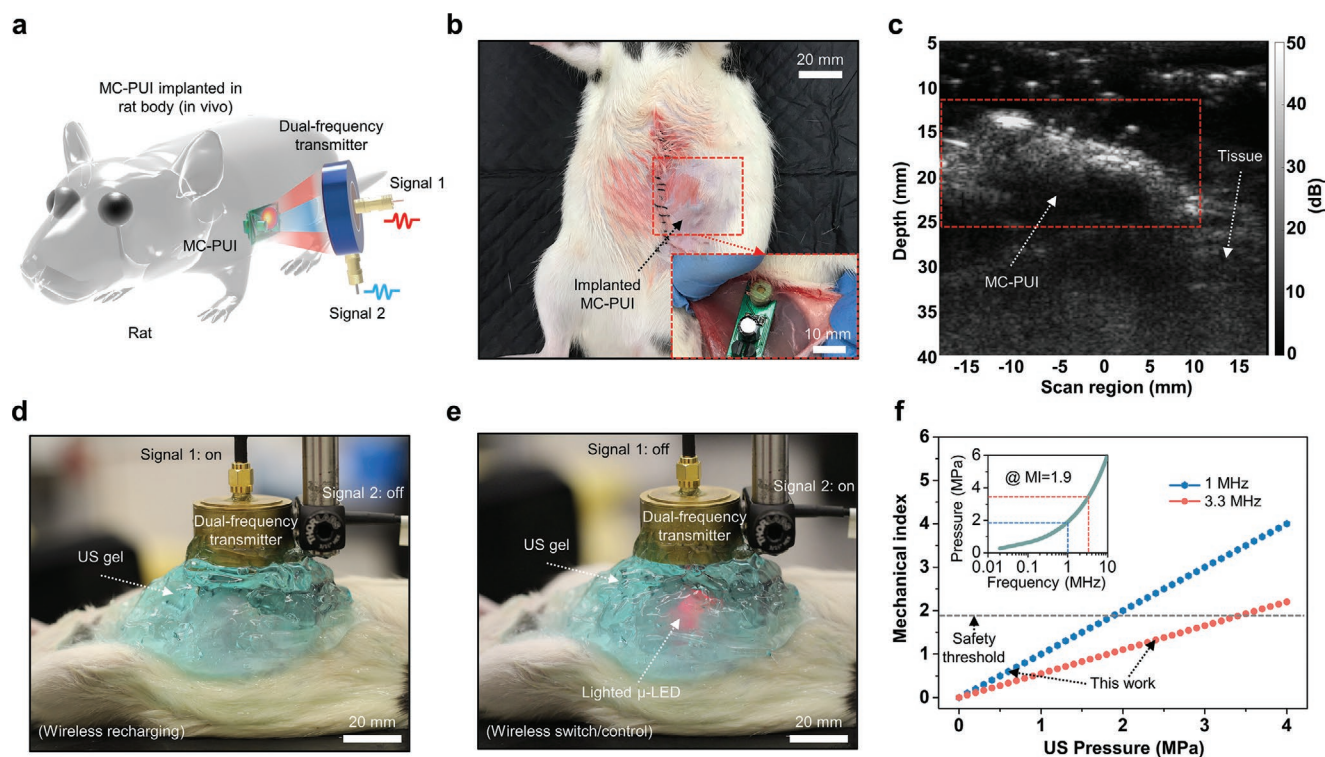


**Figure 6.** In vivo evaluation with MC-PUI implanted in a rat. a) Schematic diagram of the in vivo model showing the MC-PUI device implanted in a rat. b) Optical images showing a rat during the surgery for MC-PUI device implantation. c) US image showing the MC-PUI implanted in rat tissue. d,e) Optical images showing the in vivo experimental setup to evaluate the d) wireless charging and e) switch/control performance of the MC-PUI. f) Relationships between mechanical index (MI) and US pressure. Inset: Relationship between US pressure and frequency when the MI ( $= 1.9$ ) is at the FDA safety threshold.

by the absorption, reflection, and divergence of the ultrasonic waves, which are linearly dependent on the US frequency.<sup>[50]</sup> For example, the acoustic attenuation coefficient of muscle tissue is  $\approx 1.09 \text{ dB cm}^{-1} \text{ MHz}^{-1}$ .<sup>[51]</sup> Transcutaneous electronic implants are generally located at  $\approx 5$  to 10 mm depth. Therefore, the calculated acoustic attenuations are  $\approx -3.6$  and  $-1.09 \text{ dB}$  at 10 mm for the 3.3 and 1 MHz US used in our work (Figure 5h,i and Figure S27, Supporting Information). The experimentally measured output voltages remain  $\approx 63\%$  and  $\approx 85\%$  (Figure 5j), respectively, fitting well with the numerical simulations. Combining ex vivo experiments in two scenarios, the generated power is high enough to recharge the capacitor and turn on the switch/control circuit, showing the feasibility of transmitting power ultrasonically at MHz frequencies.

## 2.6. In Vivo Evaluation, US-Related Biological Safety, and Further Device Optimization

To test whether the MC-PUI device functions in vivo, the MC-PUI was implanted transcutaneously in an anesthetized laboratory rat (Figure 6a). For the device implantation, a sufficient area of the abdominal skin was incised to fit the device. Once the device was deployed into the tissue between the skin and the muscle, the opened skin was closed and sutured for full implantation of the device (Figure 6b). An ultrasonic image (Figure 6c) was acquired using a commercial US imaging

probe (L7-4, Philips) to locate the device, which was  $\approx 2 \text{ mm}$  deep in the tissue. In these in vivo experiments, degassed US gel was used as the coupling medium to transmit US waves, and a heating pad was used to maintain the rat's proper body temperature (Figure 6d,e). To wirelessly charge the device to obtain sufficient voltage, the 3.3 MHz US was first triggered to excite the implanted device for 5 min with an acoustic pressure of 2.4 MPa. The 3.3 MHz US was then switched to 1 MHz for wirelessly operating the integrated  $\mu$ -LED. As shown in Figure 6e, the light emitted by the  $\mu$ -LED was observed through the skin, under an inducing pressure of  $\approx 0.5 \text{ MPa}$ . This experiment demonstrates the feasibility of US frequency control in vivo. Although a previous report has demonstrated an in vivo wireless battery charging and controlling optoelectronic system that used radiofrequency (RF) inductive coupling for wireless recharging and a Bluetooth module for wireless control,<sup>[52]</sup> we introduce a new scheme for wireless charging and controlling based on frequency-controlled US transmission. The design benefits from the integration of HWAM and multiple piezoharvesters, which provides the selective characteristics of US at MHz frequencies. In comparison to RF waves, US waves have lower attenuation through tissue, a higher U.S. Food and Drug Administration (FDA) limit for power flux ( $7.2 \text{ mW mm}^{-2}$  vs  $0.1 \text{ mW mm}^{-2}$ ), better security in cybercommunications, and a much smaller wavelength (five orders of magnitude shorter at a similar frequency) for more efficient coupling to small implants.<sup>[9,53]</sup>

Despite the feasibility of frequency-controlled operations in vivo, the US-related biological safety and further device optimization are worth discussing. First, US technology has been applied for over 20 years and has an excellent safety record. Nevertheless, organisms may experience some side effects during exposure to high-intensity US, such as mechanical and thermal effects. These effects result in various tissue injuries, including altered gene expression, abnormal cell migration, necrosis, and membrane dysfunction.<sup>[54]</sup> To assess the mechanical damage, the mechanical index (MI) has been specified, which is an indication of US beam's ability to cause cavitation-related bioeffects and defined as follows<sup>[55]</sup>

$$MI = \frac{P_r}{\sqrt{f_c}} \quad (4)$$

wherein  $P_r$  is the peak negative pressure of the US in MPa and  $f_c$  is the center frequency of the US beam in MHz. A higher MI value indicates greater exposure. Currently, the FDA stipulates that diagnostic US cannot exceed an MI of 1.9. The MHz-level US selected in our work, on the one hand, can reduce the electrical impedance of the UEH, thereby increasing the power, and on the other hand, can reduce mechanical damage (Figure 6f). Combining Formula (4) and US pressure measurements using a hydrophone probe, the maximum MI was calculated to be 1.32 (at 2.4 MPa) for the 3.3 MHz charging US and 0.55 (at 0.55 MPa, switch/control threshold) for the 1 MHz switch/control US (Figure 6f), both of which are below the safety threshold. The thermal index (TI) has also been specified to assess the thermal effects by the following formula<sup>[56]</sup>

$$TI = \frac{W_p}{W_{deg}} = \frac{\min(W, I_{spta} \cdot 1 \text{ cm}^2) \cdot f}{210 \text{ mW MHz}} \text{ (in soft tissue)} \quad (5)$$

wherein  $W_p$  is the attenuated ultrasonic power at the implant depth, and  $W_{deg}$  is the estimated power required to raise the tissue equilibrium temperature by 1 °C according to a selected specific tissue model.<sup>[56]</sup> For the 3.3 MHz US used for charging (PRF: 500 Hz; acoustic pressure: 2.4 MPa), the TI was calculated to be 0.58, which is considered biologically safe operation by the British Medical Ultrasound Society.<sup>[57]</sup> 1 MHz US used for switch/control with a lower frequency and lower intensity has a smaller TI. The rising temperature measured in the experiment is less than 1 °C. Considering general implantable biomedical systems, the pulsed US with a low duty cycle could be used for energy transfer.

Second, 1–3 piezoelectric composites and hybrid acoustic metastructure were designed and fabricated as core elements. They not only enhance the device sensitivity but also provide the advantage of frequency-tunable operation. In future investigations, the acoustic–electric coupling of piezoelectric materials and frequency-selectable characteristics of artificial frequency selectors could be further improved through new material selection and structural innovation, such as biomimetic structures.<sup>[58]</sup> If the transmission and conversion efficiencies were substantially enhanced, organisms could be studied at lower intensities, and the US-related biological effects could be minimized. Additionally, novel fabrication technologies, such as multimaterial 3D and 4D printing,<sup>[59]</sup> have been developed and

could be applied to manufacture core components and even all-in-one devices.

Third, although parylene-C was uniformly deposited over the MC-PUI with complete coverage to provide encapsulation and biocompatible passivation, biocompatibility could be further optimized. In future work, more biocompatible or biodegradable electronic components, such as eco-friendly lead-free ceramics, biodegradable supercapacitors/batteries, etc., could be integrated into the devices to minimize the impacts on human health, and even tunable biodegradability could be achieved, eliminating secondary surgery for device removal.

Last but not least, this study focused on the design and implementation of the MC-PUI for wireless charging and switch/control using different US frequencies. It did not consider too much the complex circuit configuration and other applications. In future work, multifrequency components (more than two) and data processing chips could be integrated into this MC-PUI to achieve personalized electronics with multifunctions, such as in portable/mobile devices for wireless powering and data transmission, intelligent wearable/implantable bioelectronics for healthcare and physiological monitoring, and even human–machine interfaces for neural communication. Advances in nanotechnologies, microelectronics, and flexible electronics can also promote the further miniaturization and mechanical flexibility of the MC-PUI, enabling a higher level of integration and better human conformability.<sup>[17,60]</sup>

### 3. Conclusions

In summary, we have developed a compact and lightweight frequency-controllable MC-PUI that integrates the HWAM, multiple piezo-composite harvesters, and commercialized electronic components into a miniaturized circuit for selective wireless energy transfer. HWAM combines both a 3D-printed ADM and a half lambda FPR, providing the advantage of high-selectivity of US frequency at the MHz-level with high transmittance ( $\approx 83\%$ ) and a unique narrow bandwidth near 1 MHz. An apparent attenuation ( $\approx -28$  dB) in voltage amplitude was detected for the piezo-harvester channel configured with HWAM as the US frequency was switched from 1 to 3.3 MHz. Compared to the single-channel US transfer system previously reported, the developed MC-PUI achieved frequency-controlled multifunctional operations through water and tissue media, such as stable wireless charging (11.08  $\mu$ W) at 3.3 MHz and high-sensitivity wireless switch/control (threshold  $\approx 0.55$  MPa) of micro-LED/motor at 1 MHz. Such a new concept of designing multichannel and frequency-selectable US devices provides a unique solution for the emerging multifunctional wireless biomedical systems that are compact yet have more control capabilities for personalized medicine, such as in vivo diagnosis and therapy, real-time monitoring, and chronic disease monitoring and feedback.

### 4. Experimental Section

*Processing of the HWAM:* The fabrication of the HWAM can be summarized into two parts: 1) mechanical processing of the FPR; 2) 3D printing of the ADM. First, the brass FPR was machined by a lathe

(SD 400, PRAZI) to form a ring with an inner diameter of 3 mm, an outer diameter of 6.5 mm, and a thickness of 2.20 mm. 20 000 mesh sandpaper was then used to polish the finished FPR. Second, MIP-SL-based 3D-printing technology (Figure S8, Supporting Information) was used to fabricate the microchannel ADM. The ADM structure was first built using SolidWorks and then sliced with an in-house-developed “digital micromirror device (DMD)-based SL” software to create different mask patterns (Figure 2a). The patterns were projected on the resin surface to generate different 2D layers. After one layer was built and attached to the previous layer, it was peeled off from the fluorinated ethylene propylene (FEP) film on the tank to print the following layers. A total of 130 layers at 50  $\mu\text{m}$  per layer were constructed to create the ADM model. After ultrasonic cleaning in an alcohol solution, the microchannel openings of the printed sample were sealed with epoxy resin to form closed air-filled channels. The resolution of the DMD chip (Texas Instruments, Dallas) was  $1920 \times 1080$ , and the projected light intensity is  $3.16 \text{ mW cm}^{-2}$ . The photocurable resin G+ (MakerJuice Labs, KS) was selected in this work due to its low viscosity and excellent mechanical property. This particular resin, which was consisted of high tensile epoxy diacrylate ( $\approx 9000 \text{ psi}$ ) and glycol diacrylate as well as the photoinitiator, had a tensile strength of 63 MPa.

**Fabrication of the Multichannel Piezo-Harvester:** As shown in Figure 2a, a dicing-and-filling method (Tcar 864-1, Thermocarbon) was first used to manufacture the PZT (DL-52, Del Piezo Specialties)/polymer 1–3 piezo-composites consisting of regular-shaped PZT pillar arrays with epoxy filling (EPO-TEK 301, Epoxy Technology). Then, the composite sample was mechanically thinned and polished to the required thickness, and both sides of the sample were sputtered with Cr/Au (50/100 nm) electrodes using a sputtering system (NSC-3000 Sputter Coater, Nano-Master). Conductive backing layers were prepared by mixing an Ag-epoxy composite with a hardener (E-Solder 3022, Von Roll) and then cured on the bottom sides of the sputtered samples. After curing, the acoustic stacks were diced into small posts and further processed into cylindrical harvesters (UEH 1: diameter  $\approx 2.7 \text{ mm}$ ) and ring harvesters (UEH 2: inner diameter  $\approx 3 \text{ mm}$ , outer diameter  $\approx 6 \text{ mm}$ ) through the lathe. Finally, poling the harvesters was implemented for 15 min at  $2 \text{ kV mm}^{-1}$  (d.c.) in silicone oil.

**Assembly of the MC-PUI:** According to the MC-PUI design, a PCB layout was created first by using PCB design software and then implemented using commercially manufactured PCB technology (Figure S1, Supporting Information). The machined harvesters and the processed HWAM were first assembled. Insulating epoxy resin was used to bond the components to combine them into an integrated multichannel piezo-harvester. Then, the integrated multichannel piezo-harvester was aligned and directly bonded on the PCB by using a thin layer ( $\approx 20 \mu\text{m}$ ) of conductive silver paste (E-Solder 3022). After curing at  $40^\circ\text{C}$  for 4 h, capacitors, resistors, diodes, transistors, rectifiers, and  $\mu\text{-LED}$ /motor were soldered to the PCB sequentially. Finally, a  $30 \mu\text{m}$  thick parylene-C was uniformly deposited onto the entire surface of the MC-PUI as encapsulation and biocompatible passivation.

**Fabrication of the Confocal Dual-Frequency Transmitter:** The structural dimensions of the confocal dual-frequency (3.3 and 1 MHz) transmitter were first designed and optimized based on PZT ceramic (DL-48, Del Piezo Specialties) with the KLM equivalent circuit-based modeling software PiezoCAD (Figure S18 and Note S6, Supporting Information). 3.3 MHz circle piezo-plate was designed as inner transmitter 1 with a diameter of 19 mm. 1 MHz ring piezo-plate was designed as the outer transmitter 2 with an inner diameter of 21 mm and an outer diameter of 35 mm. Both the transmitters had a confocal length of 25 mm. The PZT piezo-plates with silver electrodes on both surfaces were then fixed into brass housing. Two subminiature version A (SMA) connectors were connected with the back electrodes using wires, respectively. A common ground connection was then formed via sputtering a Cr/Au (50/100 nm) electrode across the front electrodes and the brass housing. Finally,  $30 \mu\text{m}$  thick parylene-C coating was deposited onto the whole external surface of the transmitter as a protective layer.

**Material, Electromechanical, and Outputs Characterization of the MC-PUI:** The optical images were taken using a Micro-Vu Sol 161

microscope. Scanning electron microscopy (SEM) images and energy dispersive spectroscopy (EDS) were characterized by a JSM-7500 microscopy. Impedance and phase angle of the piezo-harvesters were analyzed by an impedance analyzer (4294A, Agilent). The polarization–electric field ( $P$ – $E$ ) hysteresis loops of the samples were measured by a ferroelectric measuring system (Hysteresis Version 3.1.1, Radiant Technologies). The capacitance was obtained using an inductance–capacitance–resistance digital bridge instrument (1715 LCR, QuadTech). The piezoelectric coefficient  $d_{33}$  was measured using a  $d_{33}$  meter (YE2730A, APC Products). According to the IEEE standard on piezoelectricity,<sup>[61]</sup> the electromechanical coupling coefficient  $k_t/k_{33}$  and the piezoelectric voltage coefficient  $g_{33}$  were calculated, respectively, using the following formulas

$$k_t \text{ or } k_{33} = \sqrt{\frac{\pi f_r}{2 f_a} \tan\left(\frac{\pi f_a - f_r}{2 f_a}\right)} \quad (6)$$

$$g_{33} = \frac{d_{33}}{\epsilon_{33}^T} \quad (7)$$

where the  $f_r$  and  $f_a$  are the resonant frequency and antiresonant frequency, respectively. The electrical and acoustic parameters of the PZT ceramic and fabricated composites are listed in Table S1 (Supporting Information).

The output performance of the MC-PUI was characterized by a multifunctional ultrasonic testing platform. The dual-frequency transmitter as the US source was fixed on a 5-axis machine (OptoSigma corp.). The MC-PUI as an US receiver was placed about 25 mm away from the end face of the transmitter. Both the MC-PUI and the transmitter were immersed in deionized water. The transmitter was driven by sinusoidal signals that were given via a function generator (AFG3252C, Tektronix) and then amplified ( $\approx 40 \text{ dB}$ ) via an amplifier (75A250A, AR RF/Microwave Instrumentation). The output voltages generated by the MC-PUI were directly detected using an oscilloscope (TDS 5052, Tektronix). The acoustic pressure output of the US transmitter was measured in the water tank with a hydrophone probe (HGL-1000, ONDA).

**In Vivo Feasibility Studies:** Before the experiment, the rat was anesthetized with an intraperitoneal injection of Ketamine/Xylazine ( $50$ – $90$  and  $5$ – $10 \text{ mg kg}^{-1}$ ), and maintained under sevoflurane inhalation through a nose cone. The abdominal skin was incised, and the device was implanted between the skin and the muscle. Ecoflex GEL, a well-known biocompatible silicone material, was used to encapsulate the parylene-C coating. The device adhered to the muscle with cyanoacrylate adhesive (Henkel, Dusseldorf, Germany), and the incised skin was closed with sutures. The L7-4 probe (Philips, Amsterdam, Netherlands) was used to image the implanted device. The hair in the imaging area was removed. Degassed ultrasound gel was used to couple the transmitter and the skin. All rat experiments were conducted following the protocols approved by the Animal Use and Care Committee at Huazhong University of Science and Technology.

**FEA Simulations:** The finite element analysis (FEA) technique was used to simulate the US transmission and piezoelectric potential distribution by using COMSOL Multiphysics package. The physical fields included pressure acoustic for water and air, solid mechanics for the solid structure like FP resonator and US transducer, and electrostatics used on the US transducer to enable the piezoelectric effect field. The acoustic-solid boundary was automatically applied on all boundaries between the acoustic field and solid structure field. The acoustic boundaries in propagation direction were set as an incident plane wave and perfect matching layer to simulate unrestricted propagation. The acoustic boundaries perpendicular to the propagation direction were set as the hard acoustic boundary to suppress the undesired acoustic diffraction. The parameters of piezoelectric materials were set according to the experimentally measured properties listed in Table S1 (Supporting Information). The HWAM's parameters and the geometry of piezo-composites were strictly consistent with the designs of MC-PUI shown



in Figure 2. Other parameters were chosen from COMSOL's material library. The study was conducted in the frequency domain.

## Supporting Information

Supporting Information is available from the Wiley Online Library or from the author.

## Acknowledgements

The authors thank Haochen Kang at University of Southern California for his assistance with the PCB design, Yizhe Sun at University of Southern California for his help with the dicing-and-filling process, and Jie Xing at Sichuan University for her assistance with the SEM and EDS characterizations. G.L. is supported by the Alfred E. Mann Innovation in Engineering Doctoral Fellowship.

## Conflict of Interest

The authors declare no conflict of interest.

## Author Contributions

L.J. and G.L. contributed equally to this work. L.J., G.L., and Y.C. conceived and designed experiments. L.J. prepared the piezo-composites and conducted the MC-PUI fabrication. Y.X., F.Q., and Y.C. contributed 3D printing process. L.J., G.L., Y.Y., J.L., and B.Z. performed experiments, data collection, and analysis. L.J. and G.L. performed physical modeling and simulations by PiezoCAD and COMSOL Multiphysics. L.J., G.L., and Y.C. wrote the manuscript. All authors discussed and commented on the manuscript.

## Data Availability Statement

The data that support the finding of this study are available from the corresponding author upon reasonable request.

## Keywords

acoustic metastructure, frequency-controlled implant, piezoelectric composites, selective energy transfer, ultrasound device

Received: June 2, 2021  
Revised: July 18, 2021  
Published online:

- [1] Q. Zheng, Q. Tang, Z. L. Wang, Z. Li, *Nat. Rev. Cardiol.* **2020**, *18*, 7.
- [2] M. B. Elming, J. C. Nielsen, J. Haarlo, L. Videbaek, E. Korup, J. Signorovitch, L. L. Olesen, P. Hildebrandt, F. H. Steffensen, N. E. Bruun, *Circulation* **2017**, *136*, 1772.
- [3] S. M. Won, L. Cai, P. Gutruf, J. A. Rogers, *Nat. Biomed. Eng.* **2021**.
- [4] X. Chen, F. Wang, E. Fernandez, P. R. Roelfsema, *Science* **2020**, *370*, 1191.
- [5] P. Gutruf, V. Krishnamurthi, A. Vázquez-Guardado, Z. Xie, A. Banks, C.-J. Su, Y. Xu, C. R. Haney, E. A. Waters, I. Kandela, *Nat. Electron.* **2018**, *1*, 652.
- [6] R. Hinchet, H.-J. Yoon, H. Ryu, M.-K. Kim, E.-K. Choi, D.-S. Kim, S.-W. Kim, *Science* **2019**, *365*, 491.
- [7] L. Jiang, Y. Yang, Y. Chen, Q. Zhou, *Nano Energy* **2020**, *77*, 105131.
- [8] M. A. Wood, K. A. Ellenbogen, *Circulation* **2002**, *105*, 2136.
- [9] D. K. Piech, B. C. Johnson, K. Shen, M. M. Ghanbari, K. Y. Li, R. M. Neely, J. E. Kay, J. M. Carmenta, M. M. Maharbiz, R. Muller, *Nat. Biomed. Eng.* **2020**, *4*, 207.
- [10] Z. L. Wang, L. Lin, J. Chen, S. Niu, Y. Zi, *Triboelectric Nanogenerators*, Springer, New York **2016**.
- [11] Y. Hu, Z. L. Wang, *Nano Energy* **2015**, *14*, 3.
- [12] A. J. Bandodkar, J.-M. You, N.-H. Kim, Y. Gu, R. Kumar, A. V. Mohan, J. Kurniawan, S. Imani, T. Nakagawa, B. Parish, *Energy Environ. Sci.* **2017**, *10*, 1581.
- [13] Y. Yang, H. Hu, Z. Chen, Z. Wang, L. Jiang, G. Lu, X. Li, R. Chen, J. Jin, H. Kang, H. Chen, S. Lin, S. Xiao, H. Zhao, R. Xiong, J. Shi, Q. Zhou, S. Xu, Y. Chen, *Nano Lett.* **2020**, *20*, 4445.
- [14] L. Jiang, G. Lu, Y. Yang, Y. Zeng, Y. Sun, R. Li, M. S. Humayun, Y. Chen, Q. Zhou, *Energy Environ. Sci.* **2021**, *14*, 1490.
- [15] S. Sonmezoglu, J. R. Fineman, E. Maltepe, M. M. Maharbiz, *Nat. Biotechnol.* **2021**, *39*, 855.
- [16] F. A. Duck, A. C. Baker, H. C. Starritt, *Ultrasound in Medicine*, CRC Press, Boca Raton, FL **2020**.
- [17] C. Wang, X. Li, H. Hu, L. Zhang, Z. Huang, M. Lin, Z. Zhang, Z. Yin, B. Huang, H. Gong, S. Bhaskaran, Y. Gu, M. Makihata, Y. Guo, Y. Lei, Y. Chen, C. Wang, Y. Li, T. Zhang, Z. Chen, A. Pisano, L. Zhang, Q. Zhou, S. Xu, *Nat. Biomed. Eng.* **2018**, *2*, 687.
- [18] C. Chen, Z. Wen, J. Shi, X. Jian, P. Li, J. T. Yeow, X. Sun, *Nat. Commun.* **2020**, *11*, 4143.
- [19] H. S. Wang, S. K. Hong, J. H. Han, Y. H. Jung, H. K. Jeong, T. H. Im, C. K. Jeong, B.-Y. Lee, G. Kim, C. D. Yoo, *Sci. Adv.* **2021**, *7*, eabe5683.
- [20] J. H. Han, J.-H. Kwak, D. J. Joe, S. K. Hong, H. S. Wang, J. H. Park, S. Hur, K. J. Lee, *Nano Energy* **2018**, *53*, 198.
- [21] Y. H. Jung, S. K. Hong, H. S. Wang, J. H. Han, T. X. Pham, H. Park, J. Kim, S. Kang, C. D. Yoo, K. J. Lee, *Adv. Mater.* **2020**, *32*, 1904020.
- [22] A. Bhatia, P. Peng, in *Essentials of Pain Medicine* (Eds: H. T. Benzon, S. N. Raja, S. S. Liu, S. M. Fishman, S. P. Cohen), Elsevier, New York **2018**, pp. 725–736.
- [23] G. Ma, P. Sheng, *Sci. Adv.* **2016**, *2*, e1501595.
- [24] Y. Cheng, C. Zhou, B. Yuan, D. Wu, Q. Wei, X. Liu, *Nat. Mater.* **2015**, *14*, 1013.
- [25] G. Lu, E. Ding, Y. Wang, X. Peng, J. Cui, X. Liu, X. Liu, *Appl. Phys. Lett.* **2017**, *110*, 123507.
- [26] Y. Li, C. Shen, Y. Xie, J. Li, W. Wang, S. A. Cummer, Y. Jing, *Phys. Rev. Lett.* **2017**, *119*, 035501.
- [27] N. Kaina, F. Lemoult, M. Fink, G. Lerosey, *Nature* **2015**, *525*, 77.
- [28] A. N. Norris, *Proc. R. Soc. A* **2008**, *464*, 2411.
- [29] X.-F. Li, X. Ni, L. Feng, M.-H. Lu, C. He, Y.-F. Chen, *Phys. Rev. Lett.* **2011**, *106*, 084301.
- [30] K. Melde, A. G. Mark, T. Qiu, P. Fischer, *Nature* **2016**, *537*, 518.
- [31] B. Assouar, B. Liang, Y. Wu, Y. Li, J.-C. Cheng, Y. Jing, *Nat. Rev. Mater.* **2018**, *3*, 460.
- [32] M. Grattieri, S. D. Minter, *ACS Sens.* **2018**, *3*, 44.
- [33] C. Fabry, *Ann. Chim. Ser. 7* **1899**, *16*, 115.
- [34] W. H. Bragg, W. L. Bragg, *Proc. R. Soc. London, Ser. A* **1913**, *88*, 428.
- [35] Z. Liu, X. Zhang, Y. Mao, Y. Zhu, Z. Yang, C. T. Chan, P. Sheng, *Science* **2000**, *289*, 1734.
- [36] S. A. Cummer, J. Christensen, A. Alù, *Nat. Rev. Mater.* **2016**, *1*, 16001.
- [37] K. Yu, N. X. Fang, G. Huang, Q. Wang, *Adv. Mater.* **2018**, *30*, 1706348.
- [38] Y. Yang, X. Li, M. Chu, H. Sun, J. Jin, K. Yu, Q. Wang, Q. Zhou, Y. Chen, *Sci. Adv.* **2019**, *5*, eaau9490.
- [39] Z. Cai, S. Zhao, Z. Huang, Z. Li, M. Su, Z. Zhang, Z. Zhao, X. Hu, Y. S. Wang, Y. Song, *Adv. Funct. Mater.* **2019**, *29*, 1906984.
- [40] Y. Yang, X. Li, X. Zheng, Z. Chen, Q. Zhou, Y. Chen, *Adv. Mater.* **2018**, *30*, 1704912.

- [41] X. Li, Y. Yang, L. Liu, Y. Chen, M. Chu, H. Sun, W. Shan, Y. Chen, *Adv. Mater. Interfaces* **2020**, 7, 1901752.
- [42] Z. Y. Shen, J. F. Li, R. Chen, Q. Zhou, K. K. Shung, *J. Am. Ceram. Soc.* **2011**, 94, 1346.
- [43] Z. Yang, D. Zeng, H. Wang, C. Zhao, J. Tan, *Smart Mater. Struct.* **2015**, 24, 075029.
- [44] Y. Yang, L. Tang, *J. Intell. Mater. Syst. Struct.* **2009**, 20, 2223.
- [45] W. A. Smith, *IEEE Trans. Ultrason., Ferroelectr., Freq. Control* **1993**, 40, 41.
- [46] H. L. W. Chan, J. Unsworth, *IEEE Trans. Ultrason., Ferroelectr., Freq. Control* **1989**, 36, 434.
- [47] J. Yang, H. Zhou, Y. Hu, Q. Jiang, *IEEE Trans. Ultrason., Ferroelectr., Freq. Control* **2005**, 52, 1872.
- [48] M. Z. Miskin, A. J. Cortese, K. Dorsey, E. P. Esposito, M. F. Reynolds, Q. Liu, M. Cao, D. A. Muller, P. L. McEuen, I. Cohen, *Nature* **2020**, 584, 557.
- [49] H. Ouyang, Z. Liu, N. Li, B. Shi, Y. Zou, F. Xie, Y. Ma, Z. Li, H. Li, Q. Zheng, *Nat. Commun.* **2019**, 10, 1821.
- [50] P. Narayana, J. Ophir, N. Maklad, *J. Acoust. Soc. Am.* **1984**, 76, 1.
- [51] A. A. Oglat, M. Matjafri, N. Suardi, M. A. Oqlat, M. A. Abdelrahman, A. A. Oqlat, O. F. Farhat, B. N. Alkhateb, R. Abdalrheem, M. S. Ahmad, *J. Med. Ultrasound* **2018**, 26, 123.
- [52] C. Y. Kim, M. J. Ku, R. Qazi, H. J. Nam, J. W. Park, K. S. Nam, S. Oh, I. Kang, J.-H. Jang, W. Y. Kim, J.-H. Kim, J.-W. Jeong, *Nat. Commun.* **2021**, 12, 535.
- [53] A. Baranchuk, B. Alexander, D. Campbell, S. Haseeb, D. Redfearn, C. Simpson, B. Glover, *Circulation* **2018**, 138, 1272.
- [54] H. Shankar, P. S. Pagel, D. S. Warner, *J. Am. Soc. Anesthesiol.* **2011**, 115, 1109.
- [55] T. L. Szabo, *Diagnostic Ultrasound Imaging: Inside Out*, Academic Press, San Diego, CA **2004**.
- [56] T. A. Bigelow, C. C. Church, K. Sandstrom, J. G. Abbott, M. C. Ziskin, P. D. Edmonds, B. Herman, K. E. Thomenius, T. J. Teo, *J. Ultrasound Med.* **2011**, 30, 714.
- [57] Safety Group of the British Medical Ultrasound Society, *Guidelines for the Safe Use of Diagnostic Ultrasound Equipment*, Vol. 18, The British Medical Ultrasound Society, London **2010**, p. 52–59.
- [58] W. Zhou, P. Chen, Q. Pan, X. Zhang, B. Chu, *Adv. Mater.* **2015**, 27, 6349.
- [59] H. Cui, R. Hensleigh, D. Yao, D. Maurya, P. Kumar, M. G. Kang, S. Priya, X. R. Zheng, *Nat. Mater.* **2019**, 18, 234.
- [60] Z. Huang, Y. Hao, Y. Li, H. Hu, C. Wang, A. Nomoto, T. Pan, Y. Gu, Y. Chen, T. Zhang, *Nat. Electron.* **2018**, 1, 473.
- [61] T. Meeker, *IEEE Trans. Ultrason., Ferroelectr., Freq. Control* **1996**, 43, 717.